Revealing Ionic Transfer Kinetics in Poly(3,4-Ethylenedioxythiophene)/Multi-Wall Carbon Nanotubes

Juan Su, Thomas G Petenzi, Grégory Barbillon, Catherine Debiemme-Chouvy, Laure Fillaud, Alain Pailleret, Hubert Perrot

REVEALING IONIC TRANSFER KINETICS IN POLY(3,4-ETHYLENEDIOXYTHIOPHENE)/MULTI-WALL CARBON NANOTUBES

Juan Su, [a] Thomas Petenzi, [a] Grégory Barbillon, [a,b] Catherine Debiemme-Chouvy, [a] Laure Fillaud, [a] Alain Pailleret [a] and Hubert Perrot *[a]

[a] J. Su, Dr T. Petenzi, Pr. G. Barbillon, Dr. C. Debiemme-Chouvy, Dr. L. Fillaud, Dr. A. Pailleret, Dr. H. Perrot
Sorbonne Université, CNRS, Laboratoire Interfaces et Systèmes Électrochimiques, LISE, F-75005 Paris (France)
Email: hubert.perrot@sorbonne-universite.fr
[b] G. Barbillon
EPF – Engineering School, 55 Avenue du Président Wilson, 94230 Cachan (France)

Abstract:

Binder-free electrodes are critical for advancing supercapacitor performance. Here, we explore the development of multi-wall carbon nanotubes (MWCNTs) electrodes for supercapacitors by replacing conventional non-conductive polymer binders, such as poly(vinylidene fluoride-*co*-hexafluoropropylene) (PVDF-HFP) by a conductive polymer, poly(3,4-ethylenedioxythiophene) (PEDOT). PEDOT/MWCNT composite films were synthesized and characterized in an aqueous medium using electrochemical quartz crystal microbalance (EQCM) and advanced *ac*-electrogravimetric technique to investigate their charge storage mechanisms and ionic transfer kinetics. Compared to MWCNTs/PVDF-HFP and pure PEDOT films, the PEDOT/MWCNT composite demonstrates enhanced electrochemical performance, with improved ion concentration and reduced interfacial resistance. The EQCM analysis reveals distinct mass transfer behaviors, highlighting the role of anions, cations, and free water molecules at the interface of electrodes. Ac-electrogravimetry investigation further identifies the kinetics of ion transfer and the relative concentration of each species, showing that the composite film facilitates efficient charge storage. This work provides a new insight into understanding the interfacial behavior of binder-free PEDOT/MWCNT electrode.

Introduction

Supercapacitors (SC) have been extensively investigated both in the academic and industrial fields over the last decade due to its fast charge/discharge, excellent stability and high efficiency. Multi-wall carbon nanotubes (MWCNTs) have emerged as a promising active material for supercapacitors due to their high surface area, excellent electrical conductivity, mechanical robustness, chemical stability and thermal conductivity.[1,2] They provide a three-dimensional conductive network that facilitates efficient electron transport, while their porous structure enhances ion accessibility and electrolyte diffusion. The practical application of MWCNTs often requires the use of polymer binders, such as poly(vinylidene fluoride-*co*-hexafluoropropylene) (PVDF-HFP) to ensure mechanical stability and electrode integrity.[3] However, these binders are non-biodegradable and nearly insulating polymers that limit the electrochemical performance of the electrode.[4] To address this limitation, conducting polymers (CPs) have become a prominent focus of recent research to replace the polymer binder.[5,6]

Poly(3,4-ethylenedioxythiophene) (PEDOT) is considered as an efficient CP due to its narrow bandgap, wide potential window, excellent processability and efficient integration with various materials.[7]

Previous studies have extensively explored the electrochemical properties and applications of PEDOT/MWCNTs composites, particularly in energy storage devices such as supercapacitors and batteries.[8,9,10,11] These works have demonstrated the synergistic effects of combining the high conductivity and flexibility of PEDOT with the mechanical strength and large surface area of MWCNTs, leading to enhanced electrochemical performance. However, there remains a significant gap in the literature concerning the in-depth understanding of ionic transfer kinetics. In particular, the behavior of ion transfer, the contribution of free water molecules, and the charge compensation processes in these composites have yet to be fully understood. This lack of detailed insight limits our ability to optimize these materials for high-performance energy storage applications.

Recently, electrochemical quartz crystal microbalance (EQCM)-based techniques have been wildly applied in many domains, especially for probing the interface phenomenon of various electrode/electrolyte interfaces.[12,13,14] EQCM works as a highly sensitive tool under the electrochemical working conditions, which enables simultaneous measurement of charge transfer and the corresponding mass changes for various electrodes. This powerful coupling provides direct insight into ion insertion/extraction processes, as well as solvent movement of electrode interface. Moreover, Ac-electrogravimetry (or ac-EQCM), which is a fast QCM coupling with impedance, has been developed to investigate the dynamic behavior of ion and solvent species. By analysing frequency-dependent mass and charge responses, ac-EQCM can separate different charge species (e.g., cations, anions, or solvent molecules) and identify their transfer kinetics. These features make EQCM and ac-EQCM invaluable tools for understanding charge-compensation mechanisms and ion transport dynamics in conducting polymers, carbon nanotubes, and composite electrodes.

This study aims to address this gap by employing advanced techniques such as EQCM and *ac*-electrogravimetry, to systematically analyze the ionic transfer kinetics at PEDOT/MWCNTs composites/electrolyte interface, which has not been previously reported. By combining these methods, we provide a comprehensive understanding of the mass and charge dynamics during electrochemical processes, including the roles of cations, anions, and free water molecules in the charge compensation mechanism. The EQCM allows for real-time monitoring of electrode mass changes, while *ac*-electrogravimetry offers detailed insights into the frequency-dependent behavior of ion and solvent transfer. These findings not only illustrate the fundamental mechanisms of the electrochemical performance in PEDOT/MWCNTs composites but also highlight their potential for high-performance energy storage applications.

Experimental section

Materials

Multi-wall carbon nanotubes (MWCNTs) powder (> 98 % carbon basis, outer diameter: 6-13 nm, length: 2.5-20 μm), 3,4-ethylenedioxythiophene (EDOT), sodium sulfate (Na_2SO_4), poly(vinylidene fluoride-co-hexafluoropropylene) (PVDF-HFP) and N-methyl-2-pyrrolidone (NMP, ACS reagent, assay: ≥99.0%) were

purchased from Sigma-Aldrich and used without further purification. Tetrabutylammonium hexafluorophosphate ($TBAPF_6$) was purchased from Sigma-Aldrich and recrystallized in the hot ethanol. Anhydrous acetonitrile (ACN, assay: ≥ 99.95%) was provided by VWR International L.L.C.

Materials synthesis

i) MWCNTs/PVDF-HFP films were prepared by drop-casting according to the method described in a previous work.[15] Briefly, the mixture containing 0.9 $mg \cdot mL^{-1}$ MWCNTs and 0.1 $mg \cdot mL^{-1}$ PVDF-HFP in NMP was ultrasonicated for 1 h. The suspension of 5 µL was then deposited onto the Au electrode of a quartz resonator (AWS company, Spain), and the solvent was evaporated by heating at 60°C overnight.

ii) PEDOT films were electrochemically synthesized in a 0.1 M $TBAPF_6$/ACN electrolyte containing 1 mM of the EDOT monomer. The cyclic voltammetry (CV) method was applied for the deposition at a scan rate of 100 $mV \cdot s^{-1}$ in a potential range from - 0.5 V to 1.5 V vs. Ag/AgCl for 10 cycles.

iii) For the deposition of PEDOT/MWCNTs films, 10 $mg \cdot L^{-1}$ MWCNTs were added to 20 mL of a 0.1 M $TBAPF_6$/ACN solution and ultrasonicated for 30 min. Afterwards, 1 mM EDOT monomer was added into the electrolyte. Then, the composite films were deposited by CV method by the same way as PEDOT electrodeposition.

Materials characterization

The surface of the three types of electrodes was characterized by scanning electron microscopy (SEM, Ultra55, Zeiss, Jena, Germany) operating at 10 kV and transmission electron microscopy (TEM, JEOL JEM1011, JEOL, USA) operating at 100 kV. XPS analyses were performed with an Omicron Argus X-ray photoelectron spectrometer, equipped with a monochromated AlKα radiation source (1486.6 eV). Spectra were collected using a 100-eV pass energy for the survey scan and 20 eV pass energy for the high resolution spectra. Each spectrum was measured at three different positions and atomic ratio was calculated by taking an average value. The spectra were fitted using Casa XPS software (Casa Software Ltd, U.K.). For peak fitting, a Shirley-type background was first subtracted. The peaks were fitted using a GL (30) line shape, which consists 30 % Lorentzian and 70 % Gaussian line shapes.

Electrochemical and electrogravimetric measurements

All the conventional EQCM measurements were performed using the quartz crystal microbalance (Miller oscillator, Paris, France) combined with an Autolab potentiostat (PGSTAT12). The sensor used is a quartz crystal resonator (9 MHz, AWSensors, Valencia, Spain), which consists of a thin piece of AT-cut quartz confined between a pair of Au electrodes. The film deposited on the quartz crystal resonator, a Pt grid and an Hg/Hg_2SO_4 electrode were used as the working, counter and reference electrode, respectively. After electrodeposition, all the films were characterized by the CV method at 100 $mV \cdot s^{-1}$ in a potential range of - 0.5 V to 0.5 V vs. Hg/Hg_2SO_4 in a 0.5 M Na_2SO_4 solution, while the frequency was simultaneously recorded by a frequency meter in the EQCM device. Narrow potential window was used for MWCNT/PVDF-HFP film to avoid the significant side reactions. The rigidity of each film was validated by using a precision impedance analyzer (Agilent 4294).

Agilent network analyzer is used to measure all the parameters of the equivalent circuit associated to the quartz resonator, including frequency (f), motional resistance (R_1) and motional inductance (L_1). The frequency shift (Δf) and bandwidth shift ($\Delta\Gamma$, see equation A1 in annex below) are calculated by measuring the parameters of bare quartz crystal (f, R_1 and L_1) and the quartz crystal bearing a film (f', R_1' and L_1') in the dry state (i.e., without electrolyte) and in a 0.5 M Na_2SO_4 solution, respectively. When both $\Delta\Gamma/-\Delta f$ (measured in air) and $\Delta\Gamma'/-\Delta f'$ (measured in solution) are less than 10 %, the film is considered to be rigid.[16] The mass per unit area of the film deposited on the Au electrode of the quartz sensor, Δm, is then calculated according to Sauerbrey equation (Equation 1)[17,18]:

$$\Delta f = -\frac{2 f_0}{A\sqrt{\rho_q \mu_q}} \Delta m = -k_s \Delta m \quad (1)$$

where f_0 is the fundamental frequency of the quartz crystal resonator, A is the piezoelectrical active area, μ_q is the quartz shear modulus, ρ_q is the quartz density, Δm is the mass change. The gravimetric sensitivity (k_s) was calculated as 16.3×10^7 Hz·g^{-1}·cm^2 for a 9 MHz resonator.[19]

Ac-EQCM, also called *ac*-electrogravimetry, is a coupling between fast QCM and electrochemical impedance spectroscopy (EIS) under the influence of a sinusoidal electrochemical potential. This analytical technique allows the species (ions and solvent) that are exchanged at the electrode/electrolyte interface to be identified as their relative concentrations over a potential step or their kinetic rate of transfer. Two main transfer functions were measured through a four channels frequency response analyzer (FRA, Solartron 1254), $\frac{\Delta E}{\Delta I}(\omega)$ as classical EIS and $\frac{\Delta m}{\Delta E}(\omega)$ as the mass/potential transfer function. These two transfer functions are related to the kinetics/ease of the ionic transfer and to the molecular atomic mass as it is given in Equation A2 and A3. In addition, experimental charge/potential transfer function $\frac{\Delta q}{\Delta E}(\omega)$ can be calculated from the experimental impedance transfer function (Equation A4) and also calculated theoretically (Equation A5) which can give an insight of capacitive and faradaic processes.

Results and discussions

Characterisation of the elaborated films

The microstructure and morphology of the three films were characterized by SEM and TEM as shown in Figure 1. MWCNT film, classically prepared with the PVDF-HFP binder, shows a uniform dispersion of nanotubes, forming a dense network, as seen in the SEM micrograph (Figure 1a). From the TEM micrograph (Figure 1d), it is clear that the nanotubes are randomly oriented, with smooth surfaces and hollow structures. The inner and outer diameters of the nanotubes are approximately 6-12 nm and 10-25 nm, respectively. A few nanotubes are tangled due to the effect of PVDF-HFP.

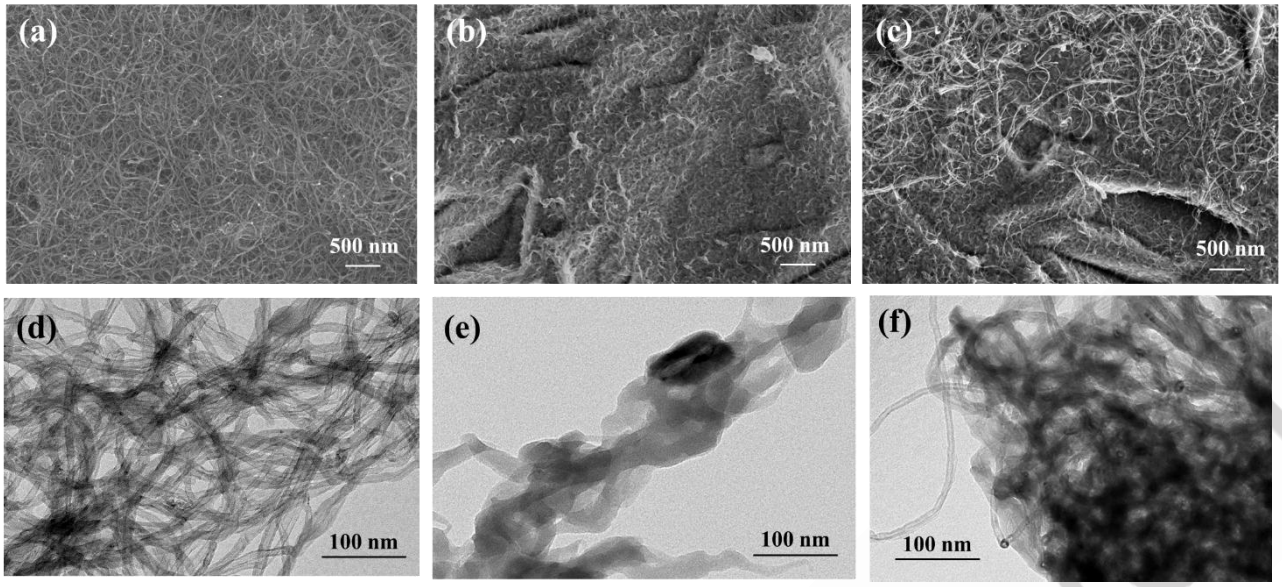

Figure 1. SEM (a, b, c) and TEM micrographs (d, e, f) of (a, d) MWCNTs/PVDF-HFP; (b, e) PEDOT; (c, f) PEDOT/MWCNT.

The surface of the PEDOT film displays a porous, sponge-like structure with visible wrinkles and clusters (Figure 1b). The porosity results from the spaces between the polymer agglomerates. Due to the rough surface of the quartz substrate, irregular cracks are observed, suggesting that the PEDOT film is very thin and exhibits a good adhesion to the substrate. In the TEM image (Figure 1e), PEDOT appears amorphous and irregular, reflecting the three-dimensional growth of long polymer chains. Darker spots represent small, agglomerated clusters.

The morphology of PEDOT/MWCNTs composite film reveals a well-integrated network structure (Figure 1c and 1f). PEDOT polymer appears as a porous, granular matrix, uniformly coating the substrate. The MWCNTs are distinctly visible, exhibiting their characteristic tubular morphology, and are dispersed on the PEDOT matrix. The composite exhibits a rough and porous surface morphology.

The XPS survey spectra and C1s fitted spectra offer a comprehensive understanding of the chemical composition and bonding states of the MWCNTs/PVDF-HFP, PEDOT, and PEDOT/MWCNTs film surface. In the survey spectra (Figure 2a), MWCNTs/PVDF-HFP exhibits a strong carbon (C1s) signal at 284 eV, characteristic peak of MWCNTs. Oxygen (O1s) peak originates from the defects on nanotube surface and nitrogen (N1s) may come from the NMP solvent residue. PEDOT film spectrum shows sulfur signals at 164 eV (S2p) and 228 eV (S2s), confirming the presence of thiophene ring. PEDOT/MWCNTs composite shows a similar survey spectrum to PEDOT film, which suggests the existence of PEDOT. As shown in Table 1, the calculated atomic ratio of C/O in the composite is lower than that of MWCNTs/PVDF-HFP but higher than that of PEDOT, and a similar trend is observed for the C/S ratio. This indicates the efficient integration of PEDOT and MWCNTs in the composite film.

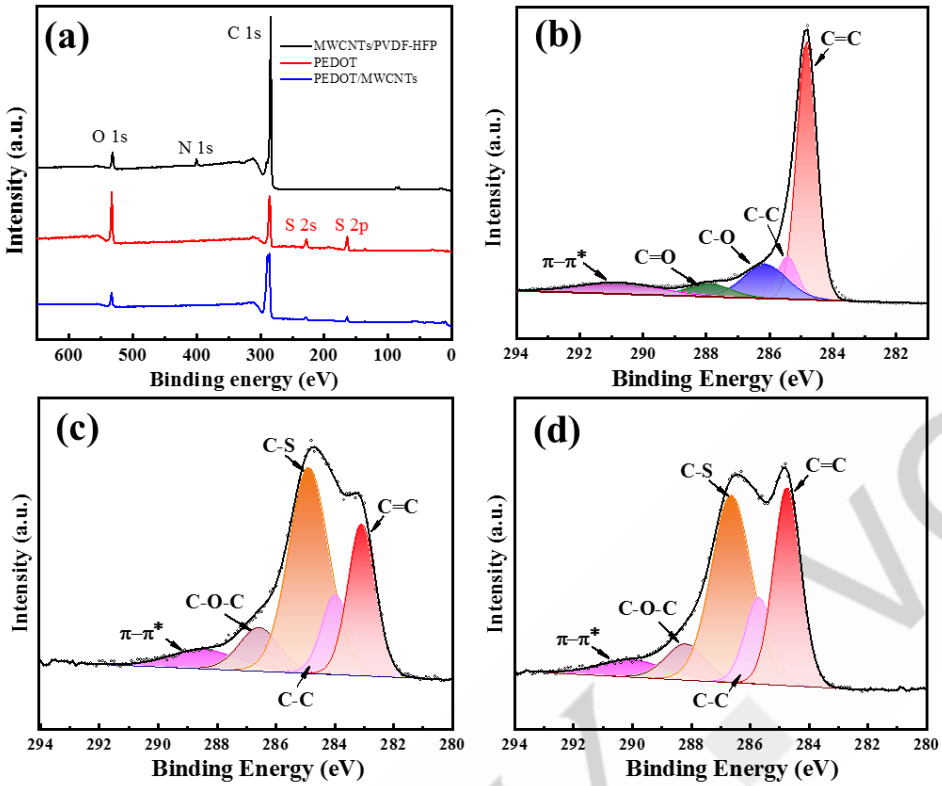

Figure 2. (a) XPS survey spectra of three films; (b) C1s spectrum of bare MWCNTs/PVDF-HFP; (c) C1s spectrum of PEDOT and (d) C1s spectrum of PEDOT/MWCNTs.

Table 1. Elemental atomic percentages of the three films obtained by XPS

Film	C (at%)	O (at%)	S (at%)	C/O	C/S
MWCNTs/PVDF-HFP	95.8	4.2	--	22.7	--
PEDOT	67.5	21.7	10.8	3.1	6.25
PEDOT/MWCNTs	70.4	19.4	10.2	3.65	6.9

Figure 2(b) shows the C1s spectrum of MWCNTs, including C=C (284.5 eV), C-C (285.0 eV), C-O (285.6 eV), C=O (288.0 eV), and π-π* (291.1 eV) contributions. For PEDOT, the C 1s spectrum (Figure 2c) reveals the contributions from C=C (283.1 eV), C-C (284.0 eV) and C-S (284.9 eV) from the thiophene rings, C-O-C (286.6 eV) from the ethylenedioxy groups and π-π* shake-up peak (288.6 eV).[20] For PEDOT/MWCNTs, the C 1s deconvolution spectra contains C=C (284.8 eV), C-C (285.7 eV), C-S (286.6 eV), C-O-C (288.2 eV) and π-π* shake-up (290.1 eV). The chemical bonding composition is similar with PEDOT, suggesting the presence of PEDOT in the composite. It is worth noted that the intensity of C=C peak in the composite is increased and C-S peak intensity is decreased compared with that in PEDOT, indicates that MWCNTs are successfully integrated with PEDOT.

Electrochemical measurements and energy storage mechanism analysis

In order to evaluate the advantages of our strategy, the electrochemical performance of three different films, i.e. MWCNTs/PVDF-HFP, PEDOT and PEDOT/MWCNTs, were tested by CV measurements in 0.5 M Na_2SO_4 aqueous solution at different scan rates from 5 to 200 $mV \cdot s^{-1}$. To clearly show the curves in the plot, 10, 20, 50, 100 and 200 $mV \cdot s^{-1}$ are selected, as shown in Figure 3(a-c). The voltage window was adapted in order to avoid the significant side reactions or film degradation.

The CV curve of MWCNTs/PVDF-HFP shows a near rectangular shape, indicating the characteristic of double-layer capacitance. A small redox peak at the potential of -0.1 ~ 0.1 V might be related to the oxygen-groups on the nanotubes.[21] For PEDOT and PEDOT/MWCNTs, the CV curves show a pseudo-rectangular shape, indicating a combination of double-layer capacitance and pseudocapacitive effects.

Based on the CV measurements, the gravimetric capacitance (C_G) can be calculated using Equation 2:

$$C_G = \frac{\int i dV}{2 m \nu \Delta V} \quad (2)$$

where i is the measured electrochemical current, m is the mass loading of the electrode estimated by QCM measurements, ν is the scan rate value of the electrochemical potential, ΔV is the voltage window. As shown in Figure 3(d), the gravimetric capacitance values of MWCNTs/PVDF-HFP, PEDOT and PEDOT/MWCNTs at a scan rate of 5 $mV \cdot s^{-1}$ are 4.0, 21.1 and 24.9 $F \cdot g^{-1}$, respectively. The specific capacitance value of PEDOT/MWCNTs is lower compared with other PEDOT/MWCNTs reports, which mainly arises from different preparation method [8,22,23] and film thickness. In this work, performances of the films are not the main interest but rather the associated electrochemical mechanism deeply investigated through EQCM advanced techniques. At each scan rate, the capacitance of the three films shows the following trend: PEDOT/MWCNTs > PEDOT > MWCNTs/PVDF-HFP. For PEDOT/MWCNTs film, the specific capacitance measured at 200 $mV \cdot s^{-1}$ still retains 56.2 % of the specific capacitance obtained at 5 $mV \cdot s^{-1}$, indicating a good rate performance.

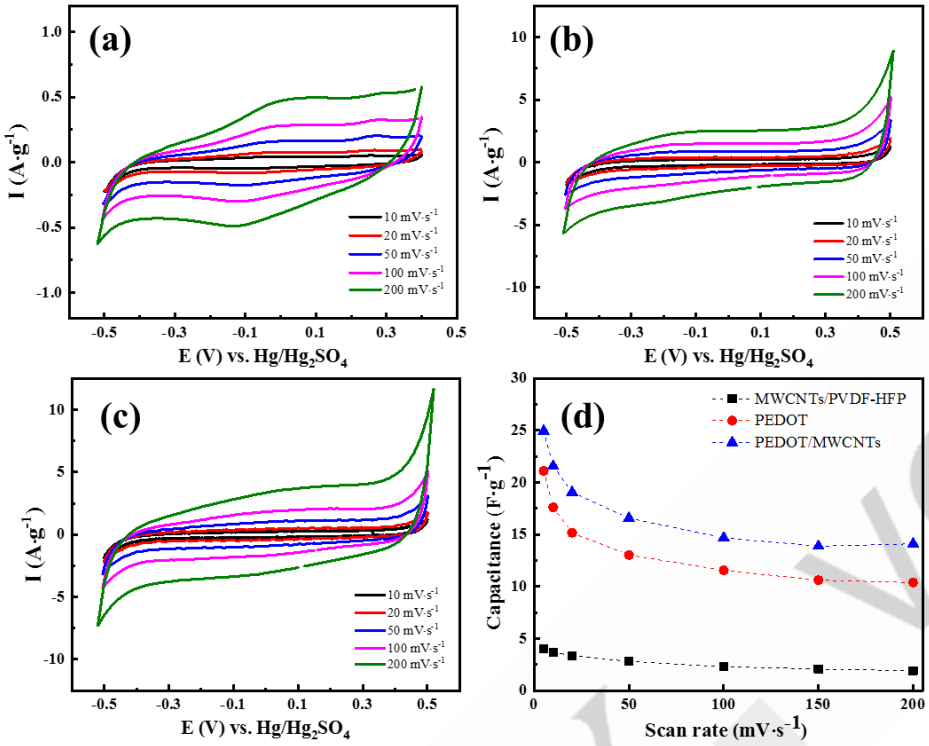

Figure 3. (a-c) Cyclic voltammograms for (a) MWCNTs/PVDF-HFP, (b) PEDOT, (c) PEDOT/MWCNTs and (d) gravimetric capacitance of these materials as a function of the scan rate, in 0.5 M Na_2SO_4 solution.

To investigate the electrochemical energy storage mechanism, the Trasatti's analysis method was used.[24,25,26,27] According to the dominated mechanism of capacitance, there are mainly two contributions: surface capacitive process and diffusion-controlled process, which means the total charge (Q_T) stored in the electrode material is attributed to the sum of charges stored at the inner (less accessible) surface (Q_{pseudo}) and outer (more accessible) surface ($Q_{surface}$). Q_{pseudo} is diffusion dependent while $Q_{surface}$ has fast ion adsorption/desorption kinetics and is independent of the potential scan rate. Therefore, the relationship between Q_T and scan rate, v, can be expressed as:

$$Q_T = Q_{surface} + Q_{pseudo} = Q_{surface} + kv^{-1/2} \quad (3)$$

In Trasatti's method, charge is used to distinguish surface capacitive and diffusion. According to the relationship between capacitance and charge ($C = \frac{\Delta Q}{\Delta V}$, in which ΔV is the applied potential range), the capacitance (C) is used in the following calculation to directly illustrate the difference of charge storage behavior. According to the C_G-$v^{-1/2}$ plot (Figure 4a), two linear fits can be clearly identified on both sides of a specific value at 20 mV·s^{-1}. When the scan rate is lower than this value, the charge storage is dominated by the fast ion adsorption/desorption. $Q_{surface}$ can be estimated by the extrapolation to the y-axis of the fitted line when $v^{-1/2}$ is zero. When the scan rate is above 20 mV·s^{-1}, C_G decreased significantly with the increase of the scan rate, indicating a diffusion-controlled ion transfer process. Meanwhile, by analyzing the C_G^{-1}-$v^{1/2}$ plot (Figure 4b), $C_{G\ total}$ can be estimated by the linear extrapolation of C_G^{-1} to the y-axis when the scan rate is zero. The contribution from surface gravimetric capacitance ($C_{G\ surface}$) and pseudo gravimetric capacitance ($C_{G\ pseudo}$) to total gravimetric capacitance ($C_{G\ total}$) is

plotted in Figure 4c for each electrode materials. For the surface capacitance, MWCNTs/PVDF-HFP film exhibits the highest double-layer capacitance due to the large surface area of MWCNTs, while PEDOT shows the lowest double-layer contribution. For the pseudo-capacitance, PEDOT dominates in pseudo-capacitance due to its reversible redox activity, whereas MWCNTs/PVDF-HFP shows the lowest Faradaic contributions. The PEDOT/MWCNTs composite achieves the highest overall capacitance by synergistically combining the double-layer capacitance of MWCNTs and the pseudo-capacitance of PEDOT, resulting in enhanced energy storage performance, which is in agreement with the capacitance shown in Figure 3d.[27,28]

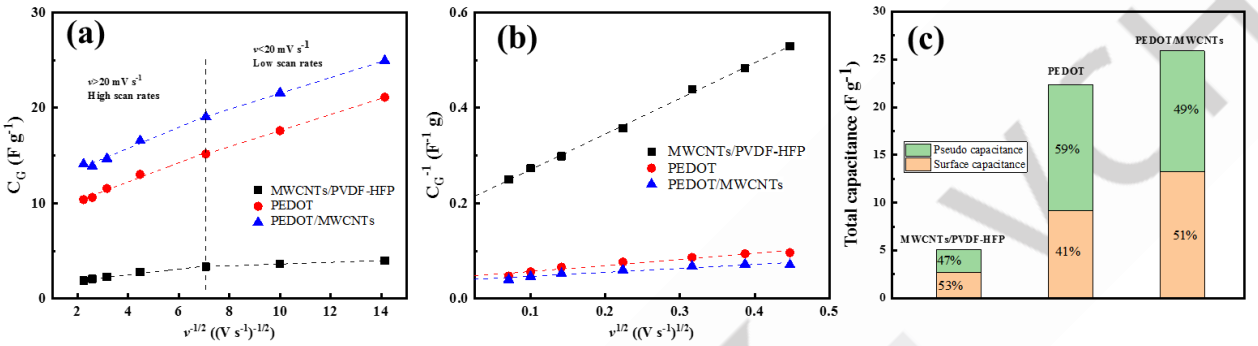

Figure 4. Analysis of the electrochemical behavior of three electrode materials: (a) Total gravimetric capacitance C_G versus $v^{-1/2}$, (b) C_G^{-1} *versus* $v^{1/2}$, (c) bar chart showing the total gravimetric capacitance with the two contributions in percentage between surface capacitive and pseudo-capacitive.

Investigation of the electrogravimetric behavior

Classical EQCM investigations

To investigate the interfacial electrochemical mechanism, microbalance frequency variations of our films, Δf, were measured simultaneously with the current, i, during electrochemical cycling (scan rate from 5 to 200 mV·s^{-1}). Then, frequencies were converted into mass variations using the classical Sauerbrey equation. The rigidity of films was demonstrated through electroacoustic impedance measurements (Table 2).[29] Two key parameters were determined following the film formation, Δf and $\Delta\Gamma$, in air and in Na_2SO_4 electrolyte. For all cases, the ratio $-\frac{\Delta\Gamma}{\Delta f}$ is under 10 % which justify the use of the Sauerbrey equation. The mass of each film was calculated as shown in Table 2. The mass difference between MWCNTs/PVDF-HFP and PEDOT film as well as PEDOT/MWCNTs film is due to the preparation method. The former was prepared by spray-coating method, while the latter two were produced via electrodeposition. Figure 5a-c shows the mass variation of the three films at various scan rate. Here, if $\frac{\Delta m}{\Delta E} < 0$, the mass change is dominated by cation exchange(s); if $\frac{\Delta m}{\Delta E} > 0$, the main contribution comes from anion exchange(s).

Table 2. Electroacoustic measurements of the three films in air and in Na_2SO_4 solution.

Film	MWCNTs/PVDF-HFP	PEDOT	PEDOT/MWCNTs
-ΔΓ/Δf (in air)	0.36%	3.83%	0.1%
-ΔΓ/Δf (in 0.5 M Na_2SO_4)	3.88%	6.62%	0.85%
Mass in air (μg)	5.99	1.15	1.28

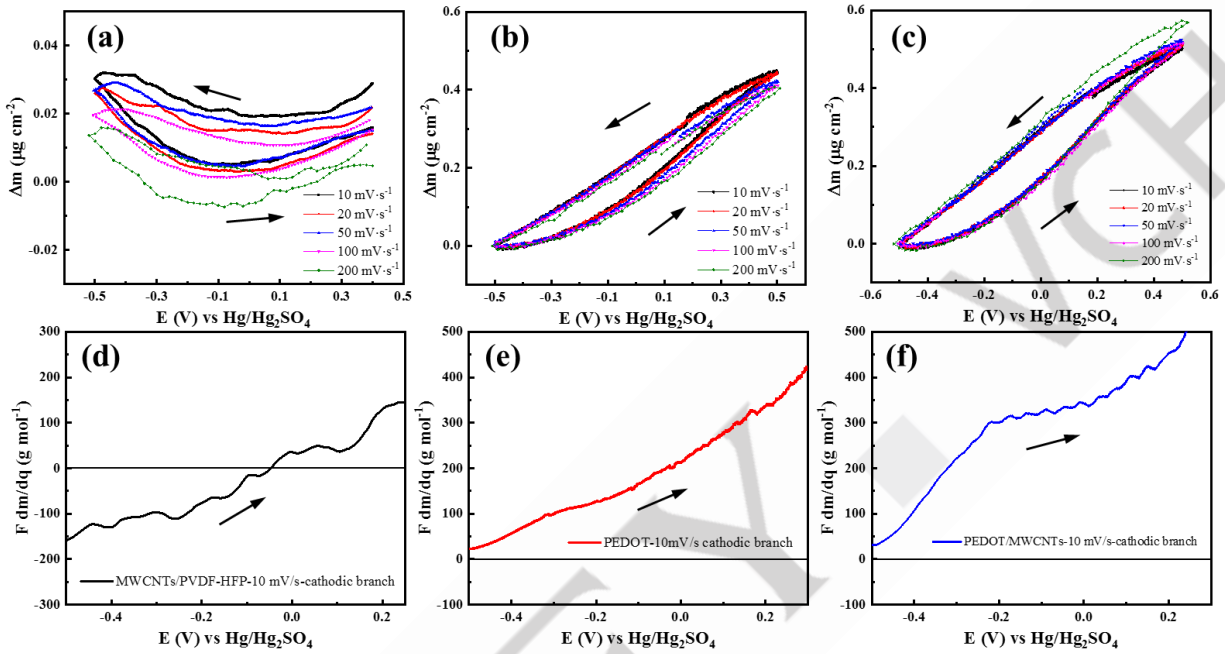

Figure 5. Mass changes and MPE of (a, d) MWCNTs/PVDF-HFP, (b, e) PEDOT and (c, f) PEDOT/MWCNTs.

For the MWCNTs/PVDF-HFP film, the mass change exhibits a distinct "V-shape" profile, suggesting that cations primarily dominate the charge compensation process at negative potentials, while anions play a dominant role at positive potentials.[30] In contrast, the mass changes of both PEDOT and PEDOT/MWCNTs films increase during the anodic scan and decrease during the cathodic scan, resulting in a positive slope. This behavior indicates that anions are the main contributors to the charge compensation process, which is in good agreement with the behavior of CP doped with small anions.[30] Notably, at each scan rate, a difference in mass change is observed between the cathodic and anodic branches, revealing a hysteresis phenomenon. This hysteresis could be attributed to the different rates of ion electro-adsorption and desorption.[31,32,33] Furthermore, the magnitude of the normalized mass change for the PEDOT/MWCNTs composite film is significantly higher than that of the PEDOT film and the MWCNTs/PVDF-HFP film. This suggests that a greater number of ions and/or free water molecules are involved in the charge compensation process for the composite film, highlighting its enhanced ion storage capacity.[34] In our studies, the mass response of PEDOT/MWCNTs is stable at different scan rates as shown in Figure 5, which is a good sight of the long-term cycle life. By this way, the stability is good enough for the EQCM and ac-EQCM measurements performed in this work.

Figure 5d-f present the values of $F\frac{dm}{dQ}$ for the cathodic branch of the three films at 10 mV·s^{-1}. This parameter, also referred to mass per electron (MPE), provides the information about the global molar mass of ions participating in the charge compensation process. $F\frac{dm}{dQ}$ can be evaluated by the following Equation:

$$MPE = F\frac{dm}{dQ} = F\frac{dm}{dt}\frac{dt}{dQ} = F\frac{dm}{idt} \quad (4)$$

where F is Faradic constant (C·mol^{-1}), dm is the mass variation (g·cm^{-2}), dQ is the charge variation (C·cm^{-2}), i is the cathodic current density (A·cm^{-2}). It is worthy to mention that the negative and positive values correspond to the cations and anions, respectively.[35] Here, for MWCNTs/PVDF-HFP film, the molar mass at the negative potentials is around 100 g·mol^{-1}, which indicates the presence of hydrated cations and/or hydrated cations with free water molecules at the same directions. While the molar mass at the positive potentials suggests anion contribution. In the case of both PEDOT and PEDOT/MWCNTs films, the MPE value across the whole potential range exhibit the main charge contribution given by anions and/or anions accompanied by free water molecules. At each potential, MPE value of PEDOT/MWCNTs films is higher than that of PEDOT film, indicating more anions are involved in the charge compensation process.

Advanced electrogravimetric investigations

To further investigate the cation, anion and free water molecule exchanged at the electrode/electrolyte interface, *ac*-electrogravimetric measurements were conducted at intervals of 0.2 V across the selected voltage window used previously for the EQCM experiments. All the *ac*-electrogravimetric data shown is obtained when the EQCM response is stable. Figure 6 shows the three main experimental transfer functions $\frac{\Delta E}{\Delta I}(\omega)$, $\frac{\Delta q}{\Delta E}(\omega)$ and $\frac{\Delta m}{\Delta E}(\omega)$ for the three films, MWCNTs/PVDF-HFP, PEDOT and PEDOT/MWCNTs film at -0.5 V *vs.* Hg/Hg_2SO_4.

As we are interested by the ionic transfer across the electrode/electrolyte interface, it is more adapted to work with another experimental transfer function, $\frac{\Delta q}{\Delta E}(\omega)$, called charge/potential transfer function. Regarding this experimental transfer function, $\frac{\Delta q}{\Delta E}(\omega)$, a large loop is observed for the three films in the same quadrant (Figure 6b, e, h). Actually, in each case, two ions are involved in the charge compensation process with a poor separation of the corresponding time constants, equivalent to the characteristic frequencies, which explain this measured flattened semi-circle. Its global diameter increases following this order: MWCNTs < PEDOT < PEDOT/MWCNTs. It indicates that the capacitive properties are expanded for the composite material which is agreement with the capacitance determined previously from a classical way (Figure 3d).

Key parameters are determined using Equations A2, A3 and A5 (see in Annex). The constants K_i and G_i, which are associated with the kinetic and the ease of transfer of each charged species, are calculated by fitting the theoretical charge/potential transfer function, $\left|\frac{\Delta q}{\Delta E}\right|^{th}(\omega)$, to the experimental one, $\left|\frac{\Delta q}{\Delta E}\right|^{exp}(\omega)$. For the three films, a good agreement is obtained in terms of loop diameter and frequency repartition.

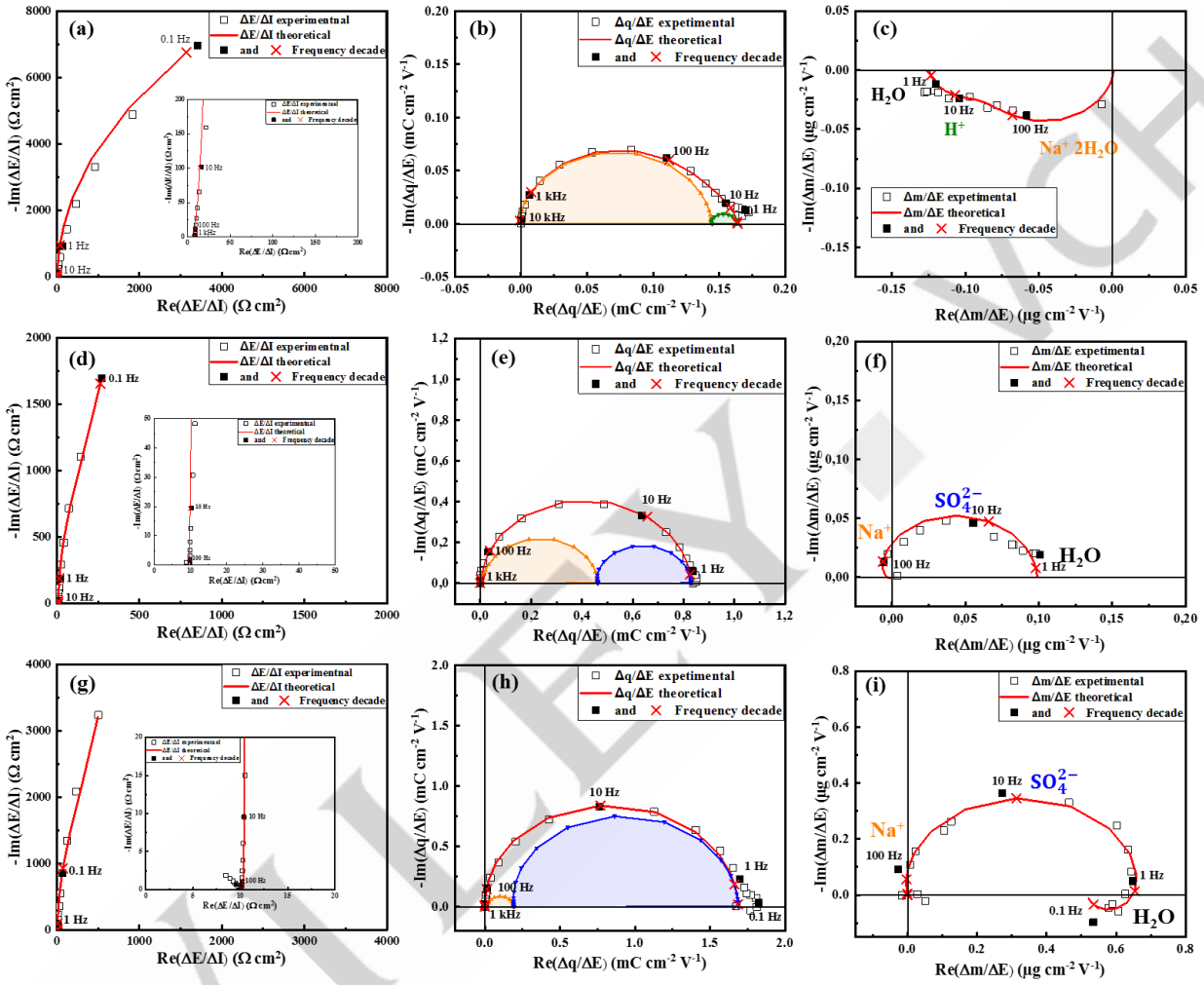

Figure 6. (a) Experimental and theoretical *ac*-electrogravimetric data of MWCNTs/PVDF-HFP (a-c), PEDOT (d-f) and PEDOT/MWCNTs (g-i) at -0.5 V vs. Hg/Hg_2SO_4, in which (a), (d) and (g) are $\frac{\Delta E}{\Delta I}(\omega)$; (b), (e) and (h) are $\frac{\Delta q}{\Delta E}(\omega)$; (c), (f) and (i) are $\frac{\Delta m}{\Delta E}(\omega)$.

In addition to identifying charged species, the $\frac{\Delta m}{\Delta E}(\omega)$ plot provides further insights into the transfer kinetics of ionic species, free water molecules. For MWCNTs/PVDF-HFP film, the $\frac{\Delta m}{\Delta E}(\omega)$ plot (Figure 6c) exhibits three species: $Na^+ \cdot 2H_2O$ transferred at high frequencies, followed by H^+ cations and H_2O molecules at low frequencies. The transfer kinetics of ions is related to their concentration in the electrolyte and their ionic radius

correlated to their ease of dehydration. In 0.5 M Na_2SO_4 electrolyte, the most common form of ions is hydrated sodium, which is detected at higher frequencies than the protons. In the latter case, due to their small radius, it is more difficult to remove the associated water molecules compared with sodium ions. Moreover, the H^+ concentrations is lower than those of Na^+ which support this lower frequency proton response. PEDOT film exhibits significantly different mass transfer behavior (Figure 6f). First, dehydrated Na^+ ions are observed at the electrode/electrolyte interface at high frequencies. It appears as a small contribution due to the lower molar mass of sodium ions compared to those of sulfate anions. Then, SO_4^{2-} move at medium frequencies, followed by free water molecules (H_2O) moving in the same direction as the anions. The same ionic species were identified for PEDOT/MWCNTs composite film, presenting an interfacial transfer kinetics of Na^+ at high frequencies, SO_4^{2-} at medium frequencies, H_2O at low frequencies in the same direction as the cations (Figure 6i). The loop size of PEDOT/MWCNTs is larger compared to those of PEDOT film, indicating that the composite film involves a higher concentration of ions in the charge compensation process.[15] This *ac*-electrogravimetric tool permits to separate the various ions/free solvent contributions in a specific way, which is not possible using classical EQCM. The three films show very distinctive responses as shown in Figure 6 in association with different ions contributions.

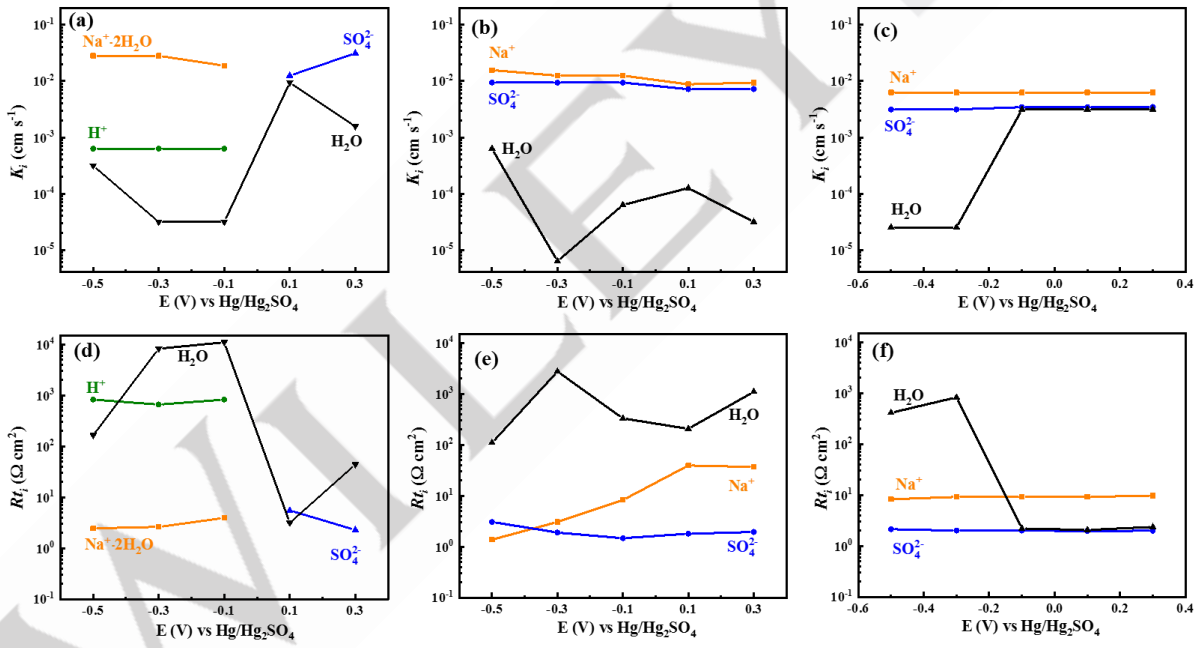

Figure 7. (a-c) Transfer kinetics, K_i, and (d-f) transfer resistance, Rt_i, of all the species as a function of the applied potential for three films: MWCNTs/PVDF-HFP (a and d), PEDOT (b and e) and PEDOT/MWCNTs (c and f).

By fitting the *ac*-EQCM results, it is possible to determine the charge transfer kinetic constants (K_i) and charge transfer resistances (Rt_i) (Equation A6) as a function of the applied potential for each of the charged and uncharged species for these three films (Figure 7). For MWCNTs, $Na^+ \cdot 2H_2O$ and H^+ were identified in the cathodic part, while SO_4^{2-} anions were detected at the anodic part. $Na^+ \cdot 2H_2O$ shows faster interfacial transfer kinetic constant and lower transfer resistance than H^+ (Figure 7a and 7d), which is in accordance with previous results about MWCNTs.[35] The case of PEDOT and PEDOT/MWCNTs films is different from that of MWCNTs,

as Na^+ and SO_4^{2-} were detected in the whole potential range (Figure 7b and 7c). The PEDOT/MWCNTs composite film exhibits lower ion transfer kinetics compared to pure PEDOT, likely due to the increased structural complexity and hindered ion mobility caused by the incorporation of MWCNTs. However, the composite film demonstrates lower overall transfer resistance (Figure 7e), attributed to the enhanced conductivity and efficient electron transfer pathways. This combination of slower kinetics and reduced resistance suggests that the composite film optimizes charge transfer efficiency, despite the trade-off in ion mobility.

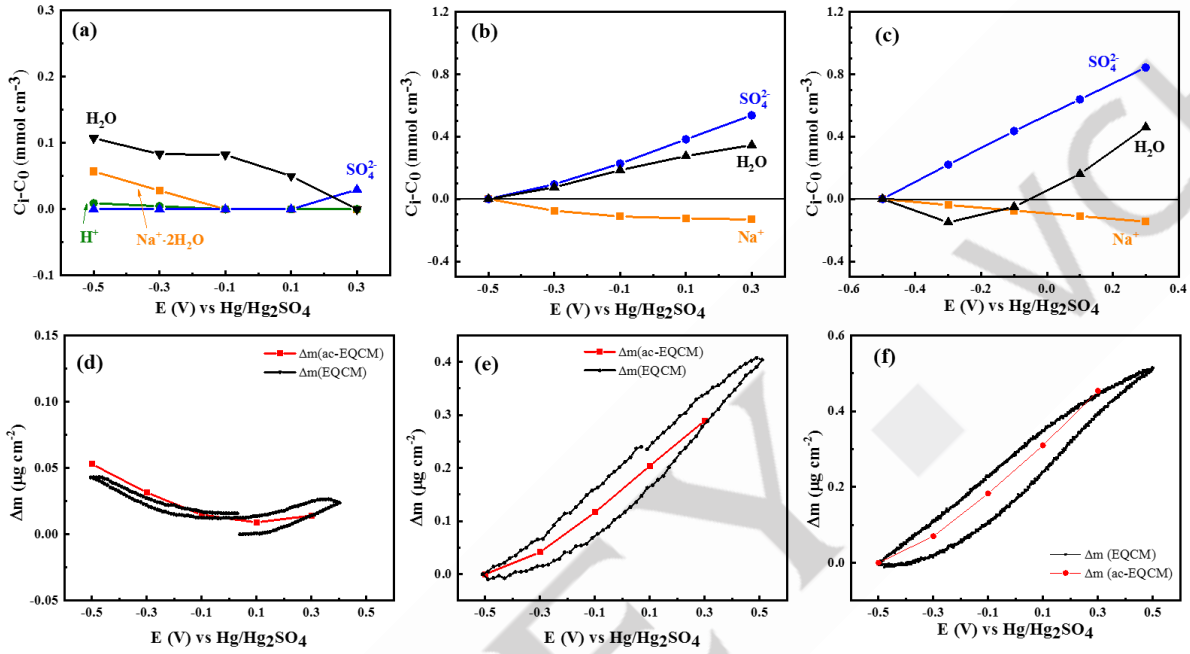

Figure 8. (a-c) Relative concentration of all transferred species and (d-f) comparison of the global mass change between EQCM and *ac*-EQCM for the three films, (a,d) MWCNTs/PVDF-HFP, (b,e) PEDOT and (c,f) PEDOT/MWCNTs.

After the estimation of the different key parameters, K_i and G_i, the relative concentration of each species was calculated at all applied potentials. Subsequently, the relative concentration $(C_i - C_0)$ of each species as a function of applied potential of each electrode film is presented in Figure 8 (a-c); it is calculated by the integration of $-\frac{G_i}{K_i}$ plot following Equations A7 (see in Annex). The MWCNTs film exhibited two cations ($Na^+ \cdot 2H_2O$ and H^+) in the cathodic potential domain and SO_4^{2-} ions at the anodic part. Both PEDOT and PEDOT/MWCNTs film displayed the decreasing concentration of Na^+ and the growing concentration of SO_4^{2-} ions as the potential increased. The global concentration of transfer species in PEDOT/MWCNTs composite film is higher compared to the other two films, indicating more charged ions are accessing the electrode/electrolyte interface, which is consistent with the electrochemical performance. The motion of H_2O molecules follows the movement of anions. This phenomenon is attributed to the electro-dragging effect of ionic flux, as reported in previous studies.[**Erreur ! Signet non défini.**,36,37] These results indicate that the electrochemical process is governed not only by ionic transfer but also by the dynamic participation of free water molecules, which significantly contribute to the observed mass variations.

With the relative concentration of all species, the mass change is reconstructed through a simple calculation using the molar mass of each species and adding the different contributions. Figure 8 (d-f) displays the mass change obtained from EQCM and reconstructed from the *ac*-EQCM results for the three electrode films. It is clearly showed that the global mass response obtained from *ac*-EQCM results is in good agreement with the data from EQCM for each film. It means that the reliability of the various parameters, m_i, K_i and G_i, given by the ac-EQCM measurements was assumed by a well-suitable cross-checking of the mass changes given directly by the EQCM and those calculated from the mentioned parameters given by the ac-EQCM. Therefore, we consider that these parameters and these results are reliable.

Conclusion

In summary, we have demonstrated the successful development of PEDOT/MWCNT composite films as a promising alternative to conventional polymer binders like PVDF-HFP. The surface morphology has been characterized by SEM and TEM. XPS analysis confirms the successful integration of MWCNTs in the electrogenerated PEDOT matrix. The energy storage mechanism analysis tells that the composite offers large ion accessible surface. Advanced techniques, like EQCM and *ac*-electrogravimetry, have been employed to investigate the charge storage mechanisms and ionic transfer kinetics of the prepared thin films. In Na_2SO_4 solution, the mass variation during the cyclic voltammetry measurements suggests anions dominate the contribution to the charge compensation process in PEDOT/MWCNTs. *Ac*-electrogravimetry provides the first insight that the synergistic effect between MWCNTs and PEDOT leads to higher concentration of ionic species in the film.

Acknowledgments

We gratefully acknowledge the financial support from the China Scholarship Council (CSC, No. 202006400017). We would also like to thank Ms. Françoise Pillier for her assistance with SEM observations and Ms. Sandra Casale for her help with TEM analysis.

Conflict of Interests

The authors declare no conflict of interest.

Data Availability Statement

The data that support the findings of this study are available from the corresponding author upon reasonable request.

Keywords: carbon nanotubes • PEDOT • binder-free • supercapacitors • EQCM • *ac*-electrogravimetry

Annex

Bandwidth shift:

$$\Delta\Gamma = \frac{R}{4\pi L} \quad \text{(A1)}$$

Electrochemical impedance or potential/current transfer function:

$$\left.\frac{\Delta E}{\Delta I}\right|_{th}(\omega) = \left(j\omega d_f F \sum_i \frac{G_i}{j\omega d_f + K_i}\right)^{-1} (i = ions) \quad \text{(A2)}$$

Mass/potential transfer function:

$$\left.\frac{\Delta m}{\Delta E}\right|_{th}(\omega) = -d_f \sum_i M_i \frac{G_i}{j\omega d_f + K_i} (i = ions\ and\ neutral\ species) \quad \text{(A3)}$$

Experimental charge/potential transfer function:

$$\frac{\Delta q}{\Delta E}(\omega) = \frac{1}{j\omega}\frac{\Delta I}{\Delta E}(\omega) \quad \text{(A4)}$$

Charge/potential transfer function:

$$\left.\frac{\Delta q}{\Delta E}\right|_{th}(\omega) = F d_f \sum_i \frac{G_i}{j\omega d_f + K_i} (i = ions) \quad \text{(A5)}$$

Transfer resistance for the species *i*:

$$Rt_i = \frac{1}{F\left|G_i\right|} \quad \text{(A6)}$$

Relative concentration for the species *i*:

$$C_i - C_0 = \int_{E_0}^{E_1} -\frac{G_i}{K_i} dE \quad \text{(A7)}$$

where:

- R is the motional resistance in the equivalent circuit associated to the quartz resonator;

- L is the motional inductance equivalent circuit associated to the quartz resonator;

- ΔE is the sinusoidally modulated electrochemical potential at the electrode/electrolyte interface;

- ΔI is the current response given by the electrochemical system;

- ω is the pulsation ($\omega=2\pi f$) with f the frequency of the sinusoidally modulated potential;

- d_f is the average film thickness;

- F is the Faraday number (96500 C·mol^{-1});

- G_i is the inverse of the transfer resistance, Rt_i, related to the ease for each species *i* to be transferred at the electrode/electrolyte interface;

- K_i is the kinetics rate of ionic/neutral species transfer across the electrode/electrolyte interface;

- Δm is the mass change related to the film measured through the QCM system;

- M_i is the molar mass of each species *i*;

- C_i-C_0 is the relative concentration change of the species *i*.

[1] S. Rathinavel, K. Priyadharshini, D. Panda, *Mater. Sci. Eng. B* **2021**, *268*, 115095.

[2] S. Zhu, J. Ni, Y. Li, *Nano Res.* **2020**, *13*, 1825–1841.

[3] Z. Su, G. Li, J. Zhang, *Adv. Funct. Mater*. **2024**, 2415409.

[4] J. Jang, J. Ahn, J. Ahn, U. Jeong, J. Yoon, J. K. Park, W. Shin, M. J. Kang, M. Cho, D. J. Kang, J. Kim, J. Yoo, H. Im, *Adv. Funct. Mater*. **2024**, *34*, 2410866.

[5] J. Kang, S. Zhang, Z. Zhang, *Adv. Mater*. **2017**, *29*, 1700515.

[6] Q. Li, Q. Zhang, J. Sun, C. Liu, J. Guo, B. He, Z. Zhou, P. Man, C. Li, L. Xie, Y. Yao, *Adv. Sci*. **2019**, *6*, 1801379.

[7] S. N. Eliseeva, M. A. Kamenskii, E. G. Tolstoyatova, V. V. Kondratiev. *Energies* **2020**, *13*, 2163.

[8] X. He, W. Yang, X. Mao, L. Xu, Y. Zhou, Y. Chen, Y. Zhao, Y. Yang, J. Xu, *J. Power Sources* **2018**, *37*, 138-146.

[9] Q. Xue, H. Gan, Y. Huang, M. Zhu, Z. Pei, H. Li, S. Deng, F. Liu, C. Zhi, *Adv. Energy Mater*. **2018**, *8*, 1703117.

[10] H. Zhou, H. Zhai, G. Han, *J. Power Sources* **2016**, *323*, 125-133.

[11] Amr M. Obeidat, A.C. Rastogi, *J. Energy Storage*, **2023**, *67*, 107563.

[12] A. Platek-Mielczarek, E. Frackowiak, K. Fic, *Energy Environ. Sci.*, **2021**, *14*, 2381–2393

[13] N. Shpigel, A. Chakraborty, F. Malchik, G. Bergman, A. Nimkar, B. Gavriel, M. Turgeman, C. N. Hong, M. R. Lukatskaya, M. D. Levi, Y. Gogotsi, D. T. Major, D.n Aurbach, *J. Am. Chem. Soc*. **2021**, *143*, 12552−12559.

[14] K. Ge, H. Shao, E. Raymundo-Piñero, P.L. Taberna, P. Simon, *Nat. Commun.*, **2024**, *15*, 1935.

[15] F. Escobar-Teran, A. Arnau, J.V. Garcia, Y. Jiménez, H. Perrot and O. Sel, *Electrochem. Commun*. 2016, *70*, 73-77.

[16] A. Bouzina, H. Perrot, C. Debiemme-Chouvy, O. Sel, *ACS Appl. Energy Mater*. **2022**, *5*, 14934-14944.

[17] Y. Ji, Z. Yin, Z. Yang, Y. Deng, H. Chen, C. Lin, L. Yang, K. Yang, M. Zhang, Q. Xiao, J. Li, Z. Chen, S. Sun, F. Pan, *Chem. Soc. Rev*. **2021**, *50*, 10743.

[18] G. Sauerbrey, *Z. Physik* **1959**, *155*, 206-222.

[19] K. Bizet, C. Gabrielli, H. Perrot, *Appl. Biochem. Biotechnol*. **2000**, *89*, 139-150.

[20] X. Chen, X. Wang, D. Fang, *Fuller. Nanotub. Carbon Nanostructures*, **2020**, *28*, 1048–1058.

[21] Li L., Li F. *New Carbon Mater*. **2011**, *26*, 224–228.

[22] K. Zhang J. Xu, X. Duan, L. Lu, D. Hu, L. Zhang, T. Nie, K. B. Brown, *Electrochim. Acta* **2014** *13*, 518-525.

[23] A. J. C. de la Torre, J. A. Á vila-Niño, R. Antaño-López, El. Araujo, *ACS Appl. Nano Mater.* **2022**, *5*, 15700–15710.

[24] S. Ardizzone, G. Fregonara, S. Trasatti, *Electrochim. Acta* **1990**, *35*, 263-267.

[25] D. Baronetto, N. Krstajić, S. Trasatti, *Electrochim. Acta* **1994**, *39*, 2359-2362.

[26] V. Augustyn, J. Come, M. A. Lowe, J. W. Kim, P. Taberna, S. H. Tolbert, H. D. Abruna, P. Simon, B. Dunn, *Nat. Mater*. **2013**, *12*, 518-522.

[27] C. Wang, F. Liu, J. Chen, Z. Yuan, C. Liu, X. Zhang, M. Xu, L. Wei, Y. Chen, *Energy Storage Mater*. **2020**, *32*, 448-457.

[28] M. Sathiya, A. S. Prakash, K. Ramesha, J-M. Tarascon, A. K. Shukla, *J. Am. Chem. Soc*. **2011**, *133*, 16291–16299.

[29] D. Johannsmann, I. Reviakine, *Nat. Rev. Methods Primers* **2024**, *4*, 63.

[30] F. Escobar-Teran, H. Perrot, O. Sel, *J. Phys. Chem. C*, **2019**, *123*, 4262−4273.

[31] S. Pruneanu, E. Csahk, V. Kertesz, G. Inzelt, *Electrochim. Acta*, **1998**, *43*, 2305-2323.

[32] G. Inzelt, *Electrochim. Acta*, **2000**, *45*, 3865-3876.

[33] A. D. Easley, K. Mohantyb, J. L. Lutkenhaus, *J. Mater. Chem. A*, **2023**, *11*, 8783–8790.

[34] Y. Wang, K. Xue, X. Zhang, X. Zhang, B. Yang, S. Xu, J. Lang, *Chem. Eng. J*. **2023**, *460*, 141704.

[35] F. Escobar-Teran, H. Perrot, O. Sel, *Materials* **2022**, *15*, 1867.

[36] A. Bouzina R. Meng, C. Bazin, H. Perrot, O. Sel, C. Debiemme-Chouvy, *Adv. Mater. Interfaces*, **2023**, *10*, 32.

[37] C. Keller, G. Barbillon, C. Debiemme-Chouvy, O. Sel, H. Perrot, *Carbon* **2024**, *227*, 119246.